BRNO UNIVERSITY OF TECHNOLOGY
VYSOKÉ UČENÍ TECHNICKÉ V BRNĚ

FACULTY OF CIVIL ENGINEERING
FAKULTA STAVEBNÍ

INSTITUTE OF STRUCTURAL MECHANICS
ÚSTAV STAVEBNÍ MECHANIKY


# STATIC AND DYNAMIC ANALYSIS OF PLAIN AND FIBER-REINFORCED CONCRETE USING DISCRETE MESO-SCALE MODEL

STATICKÁ A DYNAMICKÁ ANALÝZA PROSTÉHO A VLÁKNY VYZTUŽENÉHO BETONU S VYUŽITÍM DISKRÉTNÍHO MODELU

SHORTENED VERSION OF DOCTORAL THESIS
ZKRÁCENÁ VERZE DISERTAČNÍ PRÁCE


AUTHOR — Ing. Josef Květoň
AUTOR PRÁCE

SUPERVISOR — doc. Ing. Jan Eliáš, Ph.D.
VEDOUCÍ PRÁCE



BRNO 2019

## Key words

Concrete Fracture; Discrete modelling; Meso-scale; Fiber Reinforcement; Dynamics; Inertia; Strain-rate

© Josef Květoň
Institute of Structural Mechanics
Faculty of Civil Engineering
Brno University of Technology
Czech Republic

Typeset by LaTeX 2ε

## Bibliografic citation

KVĚTOŇ, Josef. *Static and Dynamic Analysis of Plain and Fiber-Reinforced Concrete Using Discrete Meso-Scale Model.* Brno, 2019. 93 p. Doctoral Thesis. Brno University of Technology, Faculty of Civil Engineering, Institute of Structural Mechanics. Supervised by Jan Eliáš

# Table of Contents

**1 Introductory remarks** **1**

**2 Discrete meso-scale model** **2**
2.1 Constitutive behavior . . . . . 3
2.2 Integration of stress over the facet . . . . . 7

**3 Fiber reinforced concrete** **8**
3.1 Fiber representation in computational model . . . . . 8
3.2 Fiber bridging force . . . . . 9
3.3 Micro-effects at fiber exit point . . . . . 11
3.4 Detail study on model parameters influence . . . . . 12
3.5 Comparison to experimental data . . . . . 15

**4 Dynamic concrete behavior** **16**
4.1 Balance equation - time integration . . . . . 17
4.2 Mass matrix . . . . . 18
4.3 Strain rate dependency of constitutive law . . . . . 19
4.4 Available experimental data . . . . . 20
4.5 L-shaped specimen . . . . . 20
4.6 Spalling test . . . . . 23

**5 Closing remarks** **29**
5.1 Conclusions about the fiber model . . . . . 29
5.2 Conclusions about the dynamic model . . . . . 29
5.3 Future work . . . . . 30

**References** **31**

**Curiculum vitae** **37**

**List of publications** **38**

**Abstract** **39**

# 1 Introductory remarks

In construction industry, there is a great demand on reduction of material consumption nowadays. Possibilities leading to more efficient material usage are being investigated. It is not only trend of past few years but more likely decades. Materials producing clinker minerals can be used instead of Portland cement or as its partial replacement in concrete mix. These are, for example, blast furnace slag, fly ash or silica fume [3]. Various admixtures have been introduced to improve concrete performance, for example short fiber reinforcement can lead to better tensile performance of concrete and reduction of crack width [7]. Sec. 3 is devoted to numerical modeling of fiber reinforced concrete. The reduction of material consumption can also be achieved by more detailed understanding of material behavior, which is the essential part of structural design.

Cracks and discontinuities significantly influence overall behavior and durability of structural elements, therefore it is important to understand the processes of their formation and growth. Disciplines dealing with fracture of materials were at first focused on homogeneous materials like glass or steel, where the failure can be described by linear elastic fracture mechanics. With growth of industrial production, more detailed and reliable description of material behavior is required also for heterogeneous materials. Typical heterogeneous material is concrete, where, besides relatively homogeneous cement paste, mineral aggregates appear. Their size, shape and placement within the volume affects the resulting composite quality. The fracture of concrete usually initiates from inter-facial-transition zone – ITZ (thin layer between aggregate and cement paste), which is the weakest part of material. Under increasing loading, a lot of micro-cracks grow in material. Finally some of them connect and form the macro-crack, i.e. crack localizes. The crack then propagates through the material and usually does not cross the aggregates, whose strength is considered much higher than the strength of the cement paste (for a normal strength concrete).

When developing a concrete model, it is necessary to determine at which scale it will be used. Homogeneous models are suitable for material scales where material can be simplified as homogeneous. In case of steel, this can be also applied for relatively small structural members, e.g. bolts. In case of concrete,

homogeneity assumption is widely used in case of modelling of whole buildings. The homogeneous models are typically treated as continuous. Problems treated as continuous are described by partial differential equations. An approximate solution of such problems can be provided by various numerical methods, *finite element method* (FEM) is widely used nowadays.

Besides geometric and balance equations, mechanical model needs also constitutive equation relating strain and stress. The tensile failure of quasi-brittle materials is often simulated using constitutive relation with strain-softening. The descending part of the constitutive law can be expressed by various kinds of plastic or damage models. Anytime a negative slope appears in the stress – strain relation, localization of inelastic deformation may occur. This localization phenomenon causes so called spurious mesh sensitivity – the results of the simulations are dependent on the discretization of the material body. Various regularization techniques were established to prevent this behavior [6, 5, 21].

Concrete fracture takes place at the scale, where one can distinguish individual aggregates. Material is far from homogeneous at this scale. It is therefore convenient to use a model that account for material heterogeneity. Alternatively to the continuous approach, material can be represented by a system of interconnected discrete particles. Discrete meso-scale model can be conveniently used for fracture of concrete in particular.

The aim of the thesis is to present discrete meso-scale model for concrete, describe its advantages and weak spots as well. Since it is directed towards meso-scale, it is inapplicable for structural design due to large computational demands. It is suitable for design of smaller structural parts, but primarily for detailed description of fracture processes. The thesis is structured into three parts. The first part (Sec. 2) introduces discrete approach and presents the discrete particle model used in further parts for numerical simulations. The next two parts present two modifications, representation of short fiber reinforcement (Sec. 3) and extension of the code by an implicit dynamic solver (Sec. 4).

# 2 Discrete meso-scale model

Many versions of discrete approach has been introduced in literature [40, 11, 19]. One of the first attempts was a lattice of elasto-brittle elements (Fig. 1 left)

that provides quasi-brittle behavior at macro-scale. Another option is to project material inner structure on a fine lattice model and assign the material properties accordingly (Fig. 1 center). Then one can distinguish particular material phase (aggregate, cement paste or interfacial transitional zone - ITZ) that each lattice element represents. Unfortunately, such a fine lattice model leads to a computational system with a large number of degrees of freedom (DOF), especially in 3D, which makes it inefficiently demanding. These fine models are therefore usually used for representation of small material volume only. The work in the thesis is based on the meso-scale particle model where the volume domain is discretized into a system of rigid bodies with a convex polyhedral shape (Fig. 1 right). The interaction between particles takes place on the facets, where normal, shear and rotational resistance of the contact is prescribed. The origin of this approach is attributed to work of [24]. The mathematical model used within this thesis is adopted according to [10]. Comparing fine lattice and meso-scale particle model, indisputable advantage of the later is large reduction of number of DOFs. On the other hand, more complex constitutive law needs to be used, since the lower scale phenomena are ommited.

## 2.1 Constitutive behavior

Interaction of particles is governed by constitutive relations that are applied at their contact facets. The meso-scale elastic behavior is controlled by two parameters, namely elastic modulus $E_0$ and ratio between tangential and normal

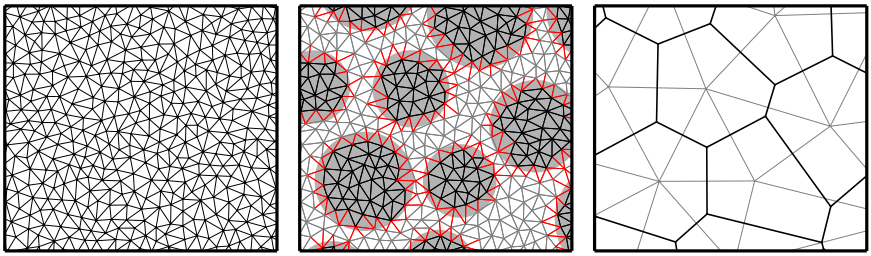

Figure 1: Various types of discrete formulation in 2D. Left: lattice of trusses or beams, center: projection of concrete structure and different element properties and right: rigid polygonal particles

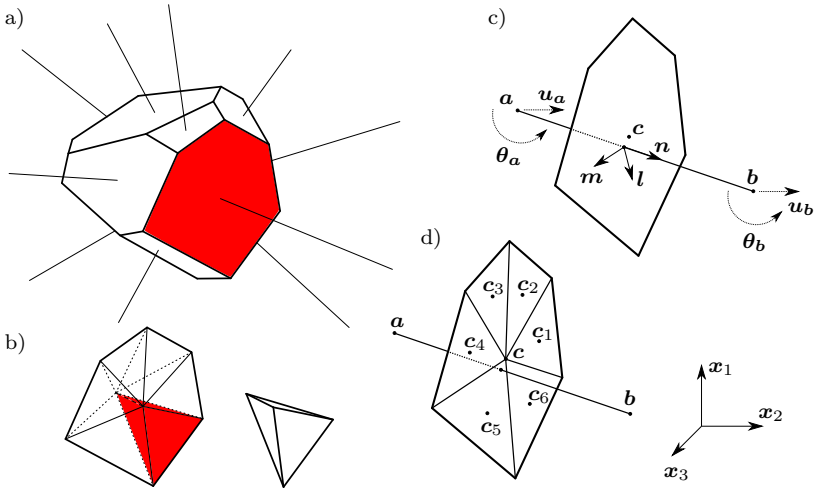


Figure 2: (a) 3D Voronoi rigid cell with connections to neighbouring particle centers, (b) decomposition of polyhedron into tetrahedrons, (c) *simple* and (d) *discretized* facet.

stiffness $\alpha$. On the contacts (facets), normal and shear stiffness of particle connection is prescribed. The kinematics of the model is provided by rigid-body motion of the particles that results in displacement jump between them. This displacement jump, divided by contact length and projected into local coordinate system, represents contact strain vector $\boldsymbol{e}$. The relation between stress $\boldsymbol{s}$ and strain $\boldsymbol{e}$ on each facet yields

$$\boldsymbol{s} = (1-D)E_0\boldsymbol{\alpha}\boldsymbol{e}\ ; \qquad D = 1 - \frac{s_{\mathrm{eq}}}{E_0 e_{\mathrm{eq}}} \tag{1}$$

where $\boldsymbol{\alpha}$ is diagonal matrix with first diagonal element equal to 1 (normal direction) and the second and third diagonal element is equal to tangential/normal stiffness ratio $\alpha$ (two shear directions). After reaching the elastic limit, the integrity of any contact is described by a damage parameter $D \in \langle 0, 1\rangle$. Zero value stands for intact material, 1 means that the contact is not able to transfer any stress. Evolution of damage $D$ is a crucial part of the constitutive law. It is calculated in an equivalent space defined by Eq. (2).

$$e_{\mathrm{eq}} = \sqrt{e_N^2 + \alpha(e_M^2 + e_L^2)} \qquad s_{\mathrm{eq}} = \sqrt{s_N^2 + (s_M^2 + s_L^2)/\alpha} \tag{2}$$

Contact behavior depends on straining direction $\omega \in \langle -\pi/2, \pi/2 \rangle$. This is calculated from local components of contact strain

$$\omega = \arctan\left(\frac{e_N}{\alpha\sqrt{e_M^2 + e_L^2}}\right) \tag{3}$$

Straining direction $\omega = -\pi/2$, 0 and $\pi/2$ indicates compressive, pure shear and tensile loading, respectively. Any angle within these limits is a combination of normal and shear loading. At first, value of the elastic limit $f_{\mathrm{eq}}(\omega)$ for a particular straining direction $\omega$ is calculated, see upper part of Fig. 3

$$f_{\mathrm{eq}} = \begin{cases} \dfrac{16 f_t}{\sqrt{\sin^2\omega + \alpha\cos^2\omega}} & \omega < \omega_0 \\ f_t \dfrac{4.52\sin\omega - \sqrt{20\sin^2\omega + 9\alpha\cos^2\omega}}{0.04\sin^2\omega - \alpha\cos^2\omega} & \omega \geq \omega_0 \end{cases} \tag{4}$$

If corresponding strain is exceeded, equivalent stress $s_{\mathrm{eq}}$ is calculated from

$$s_{\mathrm{eq}} = \min\begin{pmatrix} (1 - D_{\max}) E_0 e_{\mathrm{eq}} \\ f_{\mathrm{eq}} \exp\left(\dfrac{K}{f_{\mathrm{eq}}}\left\langle e_{\mathrm{eq}} - \dfrac{f_{\mathrm{eq}}}{E_0}\right\rangle\right) \end{pmatrix} \tag{5}$$

Here, value of maximum previously reached level of damage $D_{\max}$ provides its irreversibility and is stored for every contact individually. Initial slope $K$ of the softening/hardening curve depends on angle $\omega$, too (see lower part of Fig. 3).

$$K = \begin{cases} 0.26\, E_0 \left(1 - \left(\dfrac{\omega + \pi/2}{\omega_0 + \pi/2}\right)^2\right) & \omega < \omega_0 \\ K_t \left(1 - \left(\dfrac{\omega + \pi/2}{\omega_0 + \pi/2}\right)^{n_t}\right) & \omega \geq \omega_0 \end{cases} \tag{6}$$

Straining direction corresponding to value $\omega_0$ is on the border between softening and hardening behavior. The exponent from lower part of Eq. 6 is calculated

$$n_t = \frac{\ln(K_t/(K_t - K_s))}{\ln(1 - 2\,\omega_0/\pi)}\ ;\ K_t = \frac{2\,E_0\,f_t^2\,l}{2\,E_0\,G_t - f_t^2\,l}\ ;\ K_s = \frac{18\,\alpha\,E_0\,f_t^2\,l}{32\,\alpha\,E_0\,G_t - 9 f_t^2\,l} \tag{7}$$

where $K_t$ and $K_s$ are the initial slopes for tension and pure shear respectively. The original model has more parameters, e.g. compressive or shear elastic

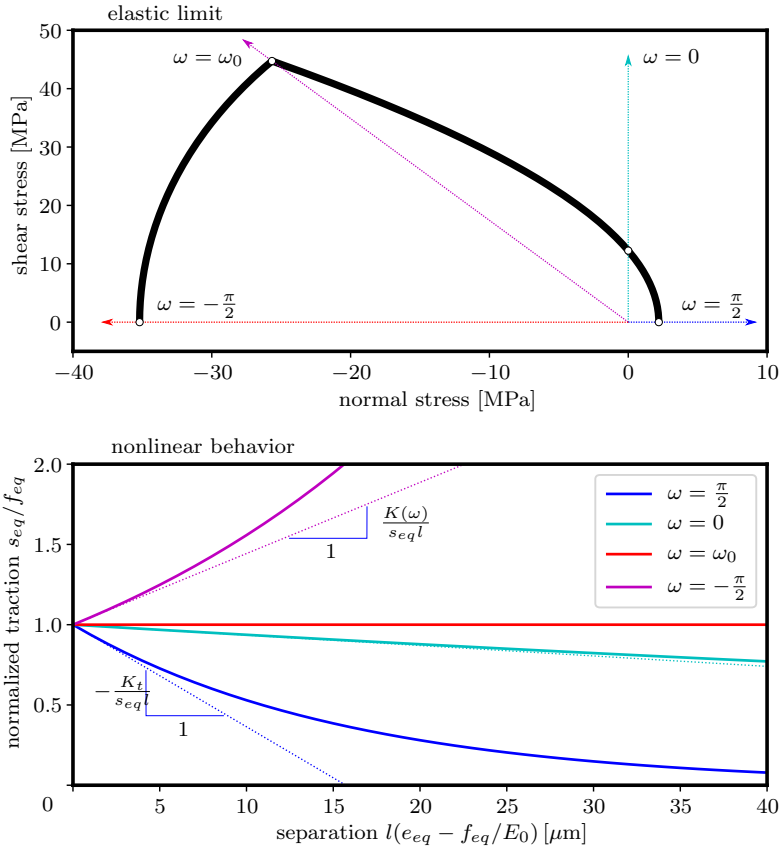


Figure 3: Top: elastic limit in terms of straining direction angle $\omega \in \langle -\frac{\pi}{2}; \frac{\pi}{2} \rangle$; bottom: different post-critical behavior for different angle $\omega$.

limits. Here, only two governing parameters for material in nonlinear regime are used, namely tensile strength $f_\mathrm{t}$ and fracture energy in tension $G_t$, the remaining parameters are derived from them according to the recommendations [10]. Constitutive law at the contact is in Eqs. (7) scaled according to the crack band approach [6] to ensure constant energy dissipation per unit contact area, independent on particle size.

Since the parameters $E_0$ and $\alpha$ are applied at meso-scale, one needs some estimation of overall material behavior observed at macro-scale. The theoretical

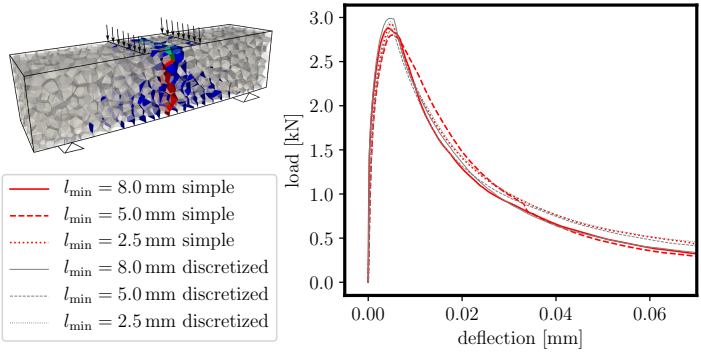


Figure 4: Difference in model results obtained for four point bending test.

relation between these meso-scale parameters and macro-scale Young's modulus and Poisson's ratio can be derived [13]. This relation reads

$$E_0 = \frac{1}{1-2\nu}E\,; \quad \alpha = \frac{1-4\nu}{1+\nu} \tag{8}$$

## 2.2 Integration of stress over the facet

A displacement jump for a single contact is calculated at the facet centroid (see Fig. 2(c)). Let us call this mechanical model *simple* facet. In this case, all the contact area is lumped into a single point, therefore rotational stiffness is neglected. Perhaps more correct approach would be to integrate stresses over the whole facet continuously accounting also for possible material nonlinearity all over the facet.

Such integration can be performed numerically introducing more integration points over the facet area, where calculation of displacement jump is performed, see Fig. 2(d). For example, polygonal facet can be decomposed into triangular sub-domains with common vertex in polygon centroid. Constitutive law is then applied in centroids of all triangles. Using such *discretized* facet, rotational stiffness is, up to some point, preserved and also possible nonlinear behavior is represented in more detail. In general, any other set of points over the facet area can be chosen. However, one should also take into account increase in computational demand with more integration points.

Difference in model results is shown on an example of four-point-bent beam in Fig. 4. Beam length is 160 mm, depth and thickness 40 mm. The simulations using *discretized* facets are predicting higher loading capacity than the ones using *simple* facets. The bending at facet level helps to resist bending at the level of whole specimen. The graphs also show that when the finer discretization is used, the influence of rotational stiffness decreases.

# 3 Fiber reinforced concrete

It is well known that plain concrete suffers from poor performance in tension. One of the possible ways of enhancing the tensile properties of concrete-based materials is to add short fibers as a reinforcement. Use of tiny fibers can lead to a significant increase in composite tensile performance. Then, the material can be used also for very thin structural members.

Various types of fiber materials are used in this field. For example, industrial floors are nowadays typically reinforced by steel fibers. The modern development of so called *engineered cementitious composites* (ECC) also reflects the advantages of plastic materials as a fiber reinforcement. Tiny *poly-vinyl alcohol* (PVA) fibers are considered as a very good choice thanks to their flexibility and rough surface promising good slip-frictional behavior. Loaded specimen is, after initial cracking, further able to transfer increasing value of load. That is the reason why they are also referred to as *strain hardening cementitious composites* (SHCC). Strain hardening behavior is obtained only if crack density is high, than, overall elongation of specimen is distributed in whole volume [2].

Amount of fibers in material volume is important. According to [16] volume fraction around 2% ensures multiple cracking with sufficient crack density, which leads to strain hardening behavior. On the other hand, excessive volume fraction reduces workability of the raw material, which can lead to formation of fiber clusters that cause reduction of bond between fibers and cement paste which results in poor composite performance.

## 3.1 Fiber representation in computational model

Short fiber reinforcement influence material behavior at the meso – or even lower – scales. Furthermore, heterogeneity of the material is increased by the

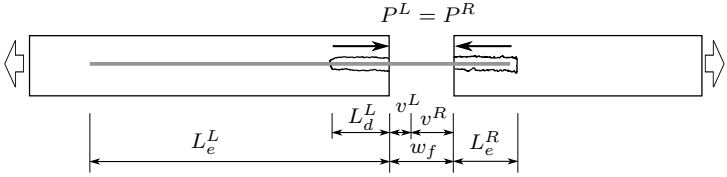


Figure 5: Crack length divided into pullout on each side according to different stage of fiber behavior – debonding on the left, pullout on the right. Superscripts $R$ and $L$ refer to the right and left side of the crack respectively.

presence of fibers. In homogeneous model, this needs to be taken into account phenomenologically.

In case of discrete meso-scale model, it appears to be convenient to take into account only frictional forces of fiber bridging crack in the material. These forces are then distributed into particles that are crossed by particular fiber [23]. In this thesis, pullout frictional resistance is for the sake of simplicity applied at contact only as a crack closing force.

For elastic behavior, fibers contribution to the stiffness of the system is neglected. Single fiber is taken into account only if it bridges any contact of particles undergoing fracture. When cracking occurs in the material, every fiber that crosses some crack is visited, bridging force is calculated and stiffness of the cracked contact is modified accordingly.

A fiber behavior is assumed to be elasto-brittle and ideally flexible. Each fiber is simplified by a straight line of a certain length. These lines are generated within volume of the specimen with prescribed or random orientation. Fibers with random orientation are directionally biased close to the boundary, because only fibers inside the specimen are allowed. If any part of generated fiber appears outside the prescribed volume domain, it is removed and a new fiber is generated instead.

## 3.2 Fiber bridging force

Phenomenological description of fiber pullout force is broadly reported in literature, though, most of the cases refer to the work of [30]. The mentioned article provides an insight into two main stages of fiber pullout, debonding and pullout slip. There is a difference between behavior of a single fiber that is

being pulled out from a material (one-sided pullout) and fiber that is bridging crack (two-sided pullout). According to [30], the following relation between pullout slip $v$ and force $P(v)$ due to fiber resistance is described [36, 43],

$$P(v) = \begin{cases} \sqrt{\frac{\pi^2 E_\mathrm{f} d_\mathrm{f}^3}{2}(\tau_0 v + G_\mathrm{d})} & \text{for} \quad v \leq v_d \\ P_0 \left(1 - \frac{v - v_d}{L_e}\right) \left[1 + \frac{\beta_\mathrm{f}(v - v_d)}{d_\mathrm{f}}\right] & \text{for} \quad v > v_d \end{cases} \tag{9}$$

$$v_d = \frac{2\tau_0 L_e^2}{E_\mathrm{f} D_\mathrm{f}} + \sqrt{\frac{8 G_\mathrm{d} L_e^2}{E_\mathrm{f} d_\mathrm{f}}} \tag{10}$$

$$P_0 = \pi L_e d_\mathrm{f} \tau_0 \tag{11}$$

Here, $d_\mathrm{f}$ denotes fiber diameter, $v$ is fiber pullout and $L_e$ is an embedment length, see Fig. 5. Parameters of the fiber constitutive law are: frictional stress between fiber and surrounding matrix $\tau_0$, fiber elastic modulus $E_\mathrm{f}$, bond fracture energy $G_\mathrm{d}$ and parameter $\beta_\mathrm{f}$ describing the slipping behavior of debonded fiber. $\beta_\mathrm{f} = 0$ refers to constant slip frictional behavior, whereas negative or positive value is used when softening respectively hardening slip behavior is considered. Critical pullout $v_d$ (pullout at complete debonding of considered fiber part) is described by Eq. (10). It has been reported that frictional behavior of fully debonded PVA fibers tends to increase [28]. This phenomenon is caused by rough surface of such fibers, that is being scraped off by surrounding material during pullout. Such behavior can be approximately characterized by positive value of parameter $\beta_\mathrm{f} > 0$.

The stated relation describes a one-sided pullout, the two-sided pullout behavior is schematically depicted in Fig. 5. A crack propagates through material over the fiber. To determine crack bridging force, crack width $w_\mathrm{f}$ is divided into two parts, belonging to each fiber part on both sides of the crack. With increasing crack width, two of the fiber parts are partially debonded ($v < v_d$). The shorter embedment lengths $L_e^R$ is fully debonded first. The debonded part is still resistant against pullout, but only due to friction between fiber and matrix – Eq. (9). Different part of crack $w_\mathrm{f}$ is assigned to pullout from the left $v^L$ or the right side $v^R$ of the crack, see Fig. 5. Calculation of bridging force is an iterative process, in which an equilibrium between forces from both sides of the crack must be reached. A simple study of two sided pullout was conducted. The contact of two particles is crossed by a fiber. The two particles have all DOFs prescribed to 0 except the right particle horizontal displacement

prescribed to $v$. The contact facet is pre-cracked from the beginning to show only the pullout representation. The influence of the model input parameters is shown in Fig. 6.

## 3.3 Micro-effects at fiber exit point

When the fiber is not parallel with the normal facet direction, micro-spalling of the cement matrix occurs in the vicinity of fiber exit point.

The embedment length is reduced of spalling length $s_\mathrm{f}$ that is, according to [36], calculated as

$$s_\mathrm{f} = \frac{P_N \sin(\theta/2)}{k_{sp} f_\mathrm{t} d_\mathrm{f} \cos^2(\theta/2)} \tag{12}$$

where $P_N$ is the normal component of crack bridging force, $k_{sp}$ is spalling coefficient, $\theta$ is angle between facet normal and fiber and $f_\mathrm{t}$ is meso-scale tensile strength of cement matrix. Inclination of fiber at exit point also causes additional friction and bearing between fiber and matrix. [36] refer to this as a snubbing effect that increases the resistance of a fiber against pullout. The following relation is used to take this phenomenon into account.

$$P_\mathrm{f} = \exp(k_{sn}\varphi'_\mathrm{f}) P(v) \tag{13}$$

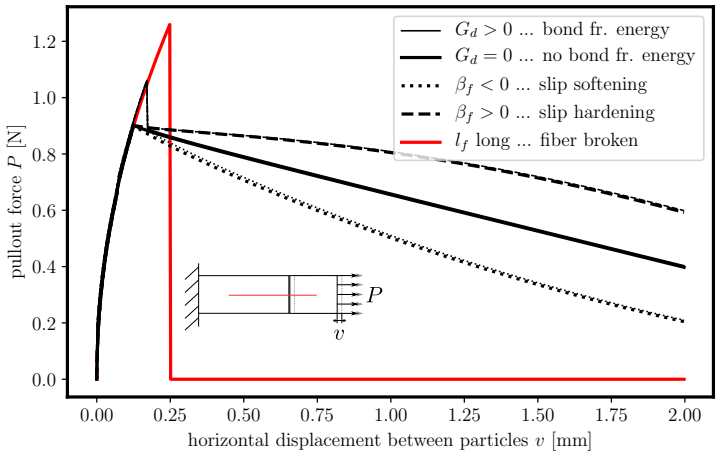


Figure 6: Influence of material parameters to results of two-sided pullout simulation.

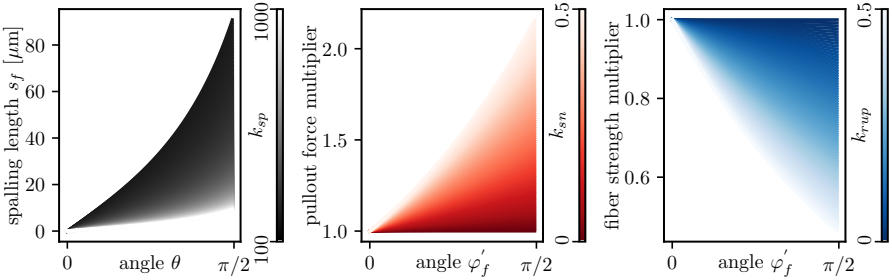


Figure 7: Influence of parameters describing micro-scale fiber behavior – Eqs. (12-14)

Here, $\varphi_{\mathrm{f}}'$ is the angle between fiber and straining direction, $k_{sn}$ is snubbing coefficient. Together with increase of the fiber pullout resistance, the fiber strength is reduced due to "bending" of an inclined fiber at the exit point [36, 43].

$$f_{tf_{\mathrm{incl}}} = f_{\mathrm{tf}} \exp(-k_{\mathrm{rup}} \varphi_{\mathrm{f}}') \tag{14}$$

where $f_{\mathrm{tf}}$ stands for fiber tensile strength and $k_{\mathrm{rup}}$ is material coefficient. The influence of parameters $k_{sp}$, $k_{sn}$ and $k_{rup}$ on the spalling length, increase of pullout force and decrease of fiber strength is shown in Fig. 7.

## 3.4 Detail study on model parameters influence

The influence of material parameters of the numerical model was studied on a simulations of the prismatic beam under uni-axial tension. Specimen length was $L = 120\,\mathrm{mm}$, width $W = 40\,\mathrm{mm}$ and thickness equal to $T = 10\,\mathrm{mm}$. Fibers of length $l_{\mathrm{f}} = 8\,\mathrm{mm}$ were used. Material parameters are the following: concrete parameters $E_0 = 48\,\mathrm{GPa}$, $\alpha = 0.237$, $f_{\mathrm{t}} = 1.5\,\mathrm{MPa}$ and $G_{\mathrm{f}} = 20\,\mathrm{J/m^2}$; fiber parameters: $E_{\mathrm{f}} = 20\,\mathrm{GPa}$, $f_{\mathrm{tf}} = 1000\,\mathrm{MPa}$, $G_{\mathrm{d}} = 5\,\mathrm{N/m}$, $\tau_0 = 2\,\mathrm{MPa}$ and $\beta_{\mathrm{f}} = 0$. Simulations using these values are plotted with magenta color.

### 3.4.1 Influence of concrete strength

The concrete strength and fracture energy was scaled as follows: $f_{\mathrm{t}h} = f_{\mathrm{t}}\, h$ and $G_{\mathrm{f}h} = G_{\mathrm{f}}\, h$. The results plotted in Fig. 8 show the influence of concrete strength to material response predicted by the numerical model. If the higher strength is assumed for concrete, the predicted loading capacity is higher. Even

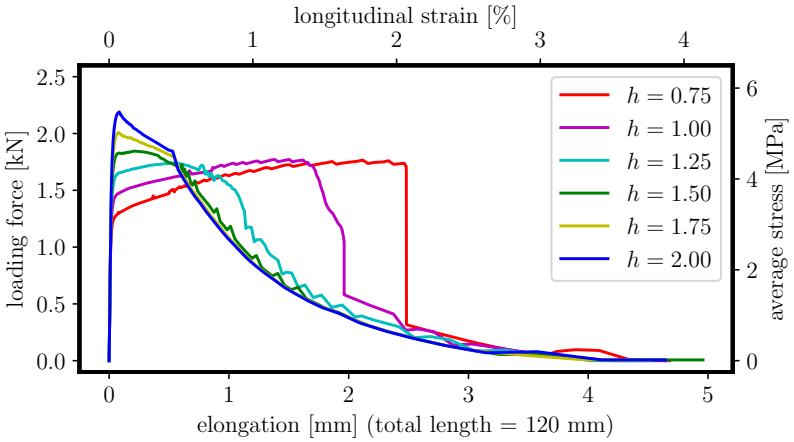


Figure 8: Influence of concrete parameters.

though the post-peak behavior is more ductile than in case of plain concrete, strain-hardening response is not obtained. This happens for simulations with lower concrete strength. In that case, multiple cracking occurs.

### 3.4.2 Influence of frictional parameters

Influence of frictional stress $\tau_0$ between fiber and matrix is addressed here. The results of simulations using wide range of values $\tau_0$ are plotted in Fig. 9. Using frictional stress $\tau_0 > 1.5\,\text{MPa}$ the model predicts strain-hardening response. We also focus on the parameter $\beta_\text{f}$ that describes increase/decrease of friction during fiber pullout and change its value to 0.5. We can see that $\tau_0$ influences mainly the initial angle of strain-hardening/softening behavior. Using positive value for parameter $\beta_\text{f}$, strain capacity predicted by the numerical model is increased. But combination of higher values of both $\tau_0$ and $\beta_\text{f}$ results into too high force that leads to fiber breakage instead of pullout.

### 3.4.3 Influence of micro-effects

In the previous simulations, influence of micro-spalling at the fiber exit point was not taken into account. In Fig. 10, various values of these parameters are used to show how they affect the model behavior. Parameters used for simu-

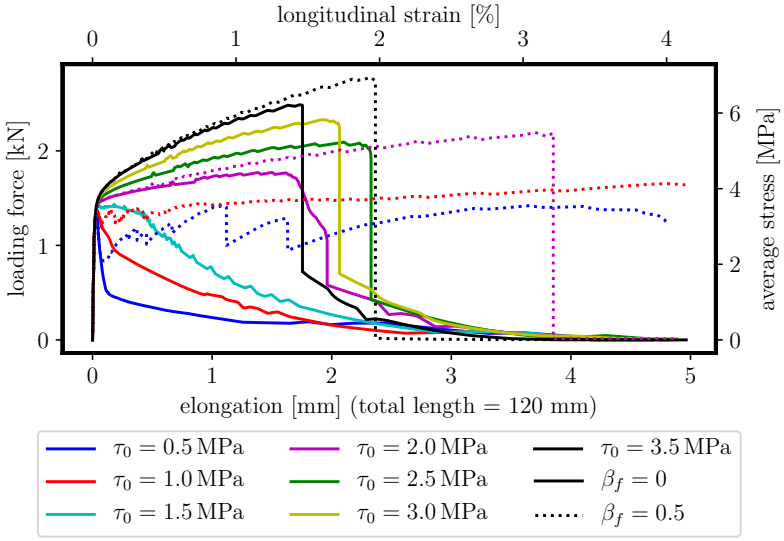


Figure 9: Influence of shear stress between fiber and matrix $\tau_0$ and hardening parameter $\beta_f$.

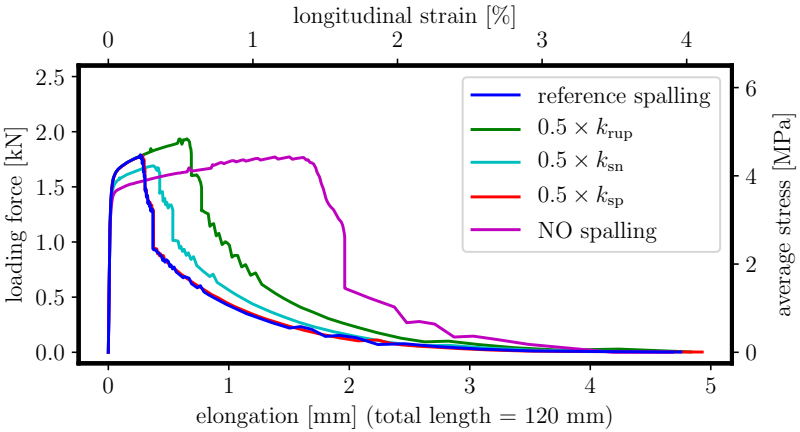


Figure 10: Influence of parameters related to micro-spalling at the fiber exit point.

lation of reference spalling were $k_{\text{rup}} = 0.33$, $k_{\text{sn}} = 0.1$ and $k_{\text{sp}} = 500$. These values are considered according to [36]. Three more calculations are performed

here, each one considering half value for one of the parameters and for comparison the calculation with no micro-effects taken into account is added. It can be observed that considering micro-effects results into prediction of higher initial peak but this also leads to earlier collapse of the simulated specimen.

## 3.5 Comparison to experimental data

Experimental series reported by [27] was chosen for comparison of the model prediction. In this series, coupon specimens of dimensions 304.8 × 76.2 × 12.7 mm were subjected to tensile tests. Fibers parameters reported in experimental series [27] are: fiber strength $f_{\mathrm{tf}} = 1\,660\,\mathrm{MPa}$, fiber elastic modulus $E_f = 42.8\,\mathrm{GPa}$, frictional stress $\tau_0 = 3.5\,\mathrm{MPa}$ and bond fracture energy $G_{\mathrm{d}} = 3.5\,\mathrm{J/m^2}$. Fiber volume fraction is $V_f = 2\,\%$, fiber diameter $d_f = 39\,\mu\mathrm{m}$ and fiber length $l_f = 12\,\mathrm{mm}$. Fibers were coated with oil to ensure their pull-

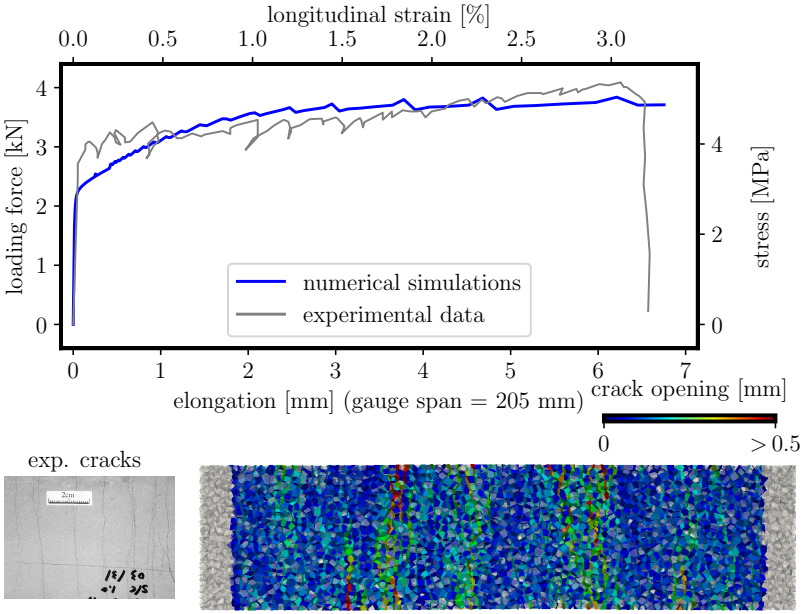


Figure 11: Comparison of the numerical load-displacement curves and crack patterns with the experimental data reported by [27].

slip behavior and prevent their breakage. The experiments with 0.3 % of oil volume content were chosen for comparison.

For numerical simulations, the geometry of the fibers, volume fraction and tensile strength were chosen according to the experimental data. The other parameter values were chosen to obtain response comparable to the experimental results. Their values are: concrete meso-scale parameter elastic modulus $E_0 = 48\,\mathrm{GPa}$, parameter $\alpha = 0.237$, tensile strength $f_\mathrm{t} = 0.75\,\mathrm{MPa}$, fracture energy $G_\mathrm{f} = 5\,\mathrm{J/m^2}$ and $l_\mathrm{min} = 3\,\mathrm{mm}$; parameters related to fiber are fiber elastic modulus $E_f = 20\,\mathrm{GPa}$, bond fracture energy $G_\mathrm{d} = 2\,\mathrm{J/m^2}$, friction $\tau_0 = 1\,\mathrm{MPa}$ and parameter $\beta = 0.05$. Parameters accounting for micro-effects at the fiber exit point $k_{sp}$, $k_{sn}$ and $k_{rup}$ are 500, 0.2 and 0.33 respectively.

The load-displacement curves of numerical simulations compared to the experiments performed by [27] are plotted in Fig. 11 together with the crack pattern. In case of quite large elongation and multiple cracking, the simulations often end up with the loss of convergence, which is considered as a final collapse. No drop is plotted in the graph, since at the last step the model terminated due to convergence problems.

# 4 Dynamic concrete behavior

Macroscopic mechanical behavior of concrete is dependent on the strain rate. Damaging specimens under higher strain rate typically leads to increase of the loading forces and energy dissipation. In case of quasi-static loading, the initial micro cracks localize into one highly damaged zone – macro crack. For higher rates, the work done by loading forces is not consumed by one crack only, but dissipates via multiple cracking and crack branching [22]. For processes that are slow, but not slow enough to be considered as quasi static, the increase in loading forces is attributed to viscous effects and can possibly be captured by strain rate dependent material properties, for high loading rates the influence of inertia forces is the main factor responsible for increase in strength and crack branching. For high strain rates, fragmentation of the material occurs. With increasing strain rate, the amount of very small fragments increases [18]. The model needs to take these small fragments into account either by modeling them directly or representing them in constitutive law phenomenologically. Direct modeling of such small particles enables more detailed description of material

behavior, but it is computationally demanding when modeling structures of reasonable dimensions. With the strain rate dependent constitutive relation that accounts for small fragments phenomenologically, the computational cost can be significantly reduced.

Such a phenomenological description can be easily provided by dynamic increase factor (DIF). With help of DIF, the material properties are usually set to fit large series of experimental results. Several examples of such approach can be found in literature [12, 26].

It is not only the strength itself that changes with high strain rate. For quasi-brittle materials like concrete, fracture energy is an important material parameter. The eurocode [1] states that the data regarding the strain rate effect on fracture energy are too incomplete to include it into model code, nevertheless, the existence of its dependency is mentioned there. Experimental data concerning also dynamic fracture energy were published e.g. by [41] or [38]. However, direct multiplication of material strength (or fracture energy) by DIF demands the constant strain rate during the investigated time period. It is therefore suitable for rough estimation of material dynamic strength only. For more detailed analysis, dynamic solution accounting for inertia forces is more suitable. Solution of material dynamic behavior with discrete meso-scale model is described hereinafter.

## 4.1 Balance equation - time integration

Simulations of material behavior under various strain-rates bring necessity of dynamic solution that consider inertia and damping forces. The calculations are performed in dynamic regime, the time dependent response is obtained from the solution of equations of motion $\boldsymbol{M}\ddot{\boldsymbol{u}}+\boldsymbol{C}\dot{\boldsymbol{u}}+\boldsymbol{K}\boldsymbol{u}=\boldsymbol{F}$ where $\boldsymbol{M}$, $\boldsymbol{C}$ and $\boldsymbol{K}$ stand for mass, damping and stiffness matrix respectively, $\boldsymbol{F}$ is a loading vector and $\boldsymbol{u}$ is vector of unknown displacements and rotations, dotted symbols represent first and second time derivative – accelerations and velocities respectively.

Equations of motion are solved using an implicit time integration scheme according to [31]. In this case, time-derivatives of accelerations and velocities

are approximated

$$\ddot{\boldsymbol{u}}_{t+\Delta t} = \frac{1}{\beta \Delta t^2} \left( \boldsymbol{u}_{t+\Delta t} - \boldsymbol{u}_t \right) - \frac{1}{\beta \Delta t} \dot{\boldsymbol{u}}_t - \left( \frac{1}{2\beta} - 1 \right) \ddot{\boldsymbol{u}}_t \tag{15}$$

$$\dot{\boldsymbol{u}}_{t+\Delta t} = \dot{\boldsymbol{u}}_t + \Delta t \left( 1 - \gamma \right) \ddot{\boldsymbol{u}}_t + \gamma \Delta t \ddot{\boldsymbol{u}}_{t+\Delta t} \tag{16}$$

Substituting Eqs. (15)-(16) into equation of motion, the following system is obtained [4]

$$\begin{aligned} \left( \boldsymbol{K} + \frac{1}{\beta \Delta t^2} \boldsymbol{M} + \frac{\gamma}{\beta \Delta t} \boldsymbol{C} \right) \boldsymbol{u}_{t+\Delta t} = \boldsymbol{F}_{t+\Delta t} + \\ \boldsymbol{M} \left( \frac{1}{\beta \Delta t^2} \boldsymbol{u}_t + \frac{1}{\beta \Delta t} \dot{\boldsymbol{u}}_t + \left( \frac{1}{2\beta} - 1 \right) \ddot{\boldsymbol{u}}_t \right) + \\ + \boldsymbol{C} \left( \frac{\gamma}{\beta \Delta t} \boldsymbol{u}_t + \left( \frac{\gamma}{\beta} - 1 \right) \dot{\boldsymbol{u}}_t + \frac{\Delta t}{2} \left( \frac{\gamma}{\beta} - 2 \right) \ddot{\boldsymbol{u}}_t \right) \end{aligned} \tag{17}$$

where on the left side, the part multiplied by unknown displacements $\boldsymbol{u}_{t+\Delta t}$ is the effective stiffness and the right-hand side is the effective loading vector. $\Delta t$ is time step length and $\beta$ and $\gamma$ are parameters of Newmark method, that should be kept within the following limits to get unconditionally stable solution $2\beta \geq \gamma \geq 0.5$ The system is in nonlinear regime damped by dissipation of energy. Such effect is considerably more important than damping due to viscous effect and friction that are collected in matrix $\boldsymbol{C}$. Therefore damping by matrix $\boldsymbol{C}$ is omitted hereinafter.

## 4.2 Mass matrix

Lumped mass matrix is commonly used in dynamic simulations. Such simplification neglects the influence of the moments of inertia and takes into account only the mass of particle concentrated in its center. Here, full mass matrix is used. Symmetric mass matrix of a single particle then consists of $6 \times 6$ values

corresponding to 3 translational and 3 rotational DOFs as follows

$$\boldsymbol{M} = \left[\begin{array}{ccc|ccc} m & & & 0 & \Delta z & -\Delta y \\ & m & & -\Delta z & 0 & \Delta x \\ & & m & \Delta y & -\Delta x & 0 \\ \hline \mathrm{s} & & & I_{xx} & -I_{xy} & -I_{xz} \\ & \mathrm{y} & & -I_{xy} & I_{yy} & -I_{yz} \\ & & \mathrm{m} & -I_{xz} & -I_{yz} & I_{zz} \end{array}\right] \tag{18}$$

where $m$ stays for particle mass $m = \rho\, V$, $\Delta x$, $\Delta y$ and $\Delta z$ describes positional shift between particle gravity center and Voronoi node in terms of global coordinates $x$, $y$ and $z$ and the lower right sub-matrix consists of moments and product of inertia calculated according to [39]. Since the mass matrix is based on the geometry of rigid particles and the fracture is allowed only on their contacts, the matrix itself is considered constant during the whole solution time.

## 4.3 Strain rate dependency of constitutive law

The discrete model is able to capture some part of strain rate dependency at macroscopic level by correctly accounting for heterogeneity and inertia in the meso-structure. However, since used resolution does not capture all the possible cracking in the material undergoing fast damage and also viscous effect of free water in the material are not explicitly addressed, some strain rate dependency needs to be incorporated phenomenologically. To account for inertia of the interparticle material in inelastic regime, the constitutive behavior of contact facets is enriched by dependency on difference in velocities of particles it connects. Calculation of $s_{\mathrm{eq}}$ takes into account rate of crack opening, $\dot{w}$, of contact element through increase function $F(\dot{w})$ provided [9].

$$s_{\mathrm{eq}} = F(\dot{w}) f_{\mathrm{eq}} \exp\left(\frac{K}{f_{\mathrm{eq}}} \left\langle e_{\mathrm{eq}} - \frac{F(\dot{w}) f_{\mathrm{eq}}}{E_0} \right\rangle\right) \tag{19}$$

$$F(\dot{w}) = 1 + c_1 \mathrm{arcsinh}\left(\frac{\dot{w}}{c_0}\right) \tag{20}$$

where variables $c_0$ and $c_1$ are additional material parameters.

## 4.4 Available experimental data

Experimental data regarding increase in compressive strength are quite abundantly reported in literature already since the half of $20^{\text{th}}$ century, e.g. [29]. On the other hand, data qualifying tensile properties of concrete under different strain-rates, especially when concerning more information than simply dynamic tensile strength, are quite limited.

Very little experiments using conventional techniques for testing of concrete tensile properties are published. As an example, experiments on concrete L-shaped specimens or compact tension tests can be found [34]. These test are performed in dynamic regime under relatively low loading rates, up to 2.4 m/s and simulated here with the discrete meso-scale model.

More convenient technique for estimation of high-rate tensile strength using Hopkinson Pressure Bar setup [8] is based on imposing pressure on a concrete bar that finally breaks in tension after the compressive wave is reflected at the rear face as a tensile stress wave.

## 4.5 L-shaped specimen

In this section, simulations of the experimental series of concrete specimens with a shape of an upside down letter L [33] are presented. Specimen dimensions are $W, D = 500\,\text{mm}$ and $W_1, D_1 = 250\,\text{mm}$ (Fig. 12-right). Specimen thickness is $t = 50\,\text{mm}$. Depth of the bottom support is 100 mm and loading is applied by prescribed displacement in a distance of 30 mm from the edge of the specimen. The loading is applied via rigid plate that can freely rotate. The loading force is calculated during the simulations. Loading rates are chosen according to [33] as 0.25 mm/s for quasi-static loading and 0.1, 0.35, 0.74, 1.0 and 2.4 m/s to study influence of the strain-rate. Material parameters are also taken from [33]. Macroscopic Young's modulus is $E = 32.2\,\text{GPa}$ and Poisson's ratio is $\nu = 0.18$; the elastic meso-scopic parameters at the interparticle contacts are obtained from Eq. (8): meso-scale elastic modulus $E_0 = 50$ GPa and normal-tangential stiffness ratio $\alpha = 0.237$, respectively. Further material properties taken from [33] are: material density $\rho = 2210\,\text{kg/m}^3$ and tensile strength $f_\text{t} = 3.12\,\text{MPa}$. The meso-scopic fracture energy for tensile failure was identified from the quasi-static loading rate according to the experiments as $G_\text{f} = 35.5\,\text{N/m}^2$.

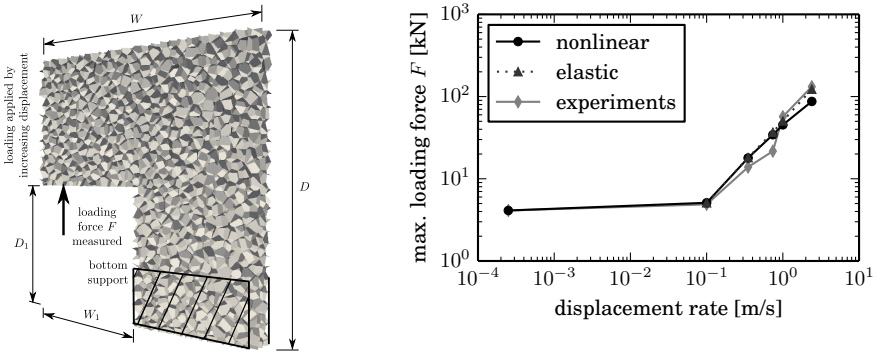


Figure 12: Left: geometry of L-shaped specimen, right: change in loading force according to displacement rate

It is interesting to compare the results with simulations considering elastic material. In Fig. 12, elastic and nonlinear responses are compared with experiments from [33]. A theoretical maximum load for elastic simulations would be in infinity, but the time dependent response oscillates around the static response, here the first such wave is considered as a peak load. Comparing the elastic calculation with the experimental response, it seems that material in the whole measured response is purely elastic. The cracking in the corner of the specimen happens later when the loading wave reaches the corner. For higher rates, the nonlinear model prediction of the peak load is affected by crushing of the material close to the loading point. Trying to avoid this crushing, gradual increase in displacement rate $v$ is applied. Using this gradual increase, the crushing in the area of applied load is reduced, but longer initial transition period $t_0$ causes reduction of loading forces, because the mass is actually accelerated under lower rate.

To show this effect of strength and fracture energy in detail, these are scaled similarly to application of spatial material randomness $h(\boldsymbol{x}) = m$, where $m$ is a strength multiplier. From load displacement curves in Fig. 13, one can observe that the value of the peak load for quasi-static rates is largely influenced, whereas the effect for other loading rates is substantially lower, especially for loading velocity 0.35 m/s. For higher rate, the dependency is caused by crushing at the loading area. In the same figure, the crack patterns are plotted at

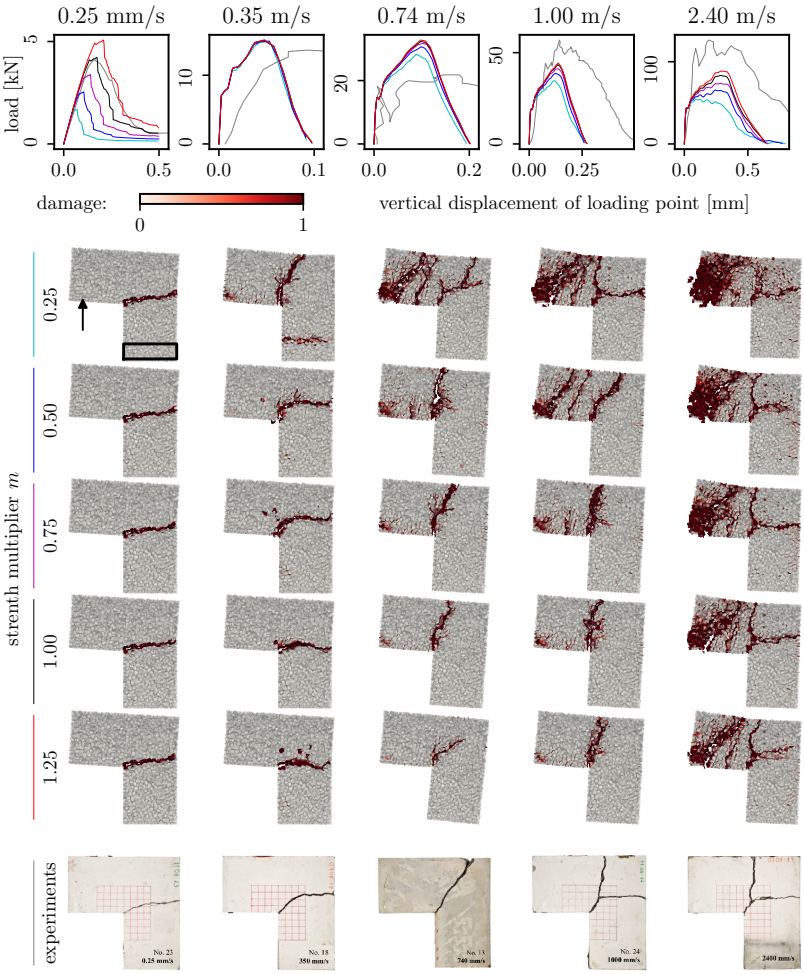


Figure 13: Load–displacement curves and crack patterns for different material strength used in numerical simulations compared with experimental data reported by [33].

the end of each simulation. The crack pattern changes with increasing rate. For quasi-static loading, the crack propagates in the horizontal direction. With an increasing rate, the inclination angle grows up to the vertical direction and crack branching occurs. These results correspond to experimental observations

[33] added in Fig. 13 in the bottom row. Comparing crack patterns for different scaling parameter $m$, weaker material results in greater inclination angle of crack direction and also crack branching occurs at lower loading velocity than for stronger material.

L-shaped specimens loaded by several displacement rates according to experiments by [33] are simulated. The peak load is highly influenced by inertia (i.e. by accelerating the mass above the loading point), while the crack pattern is highly influenced by material fracture properties. Contrary to the experimental evidence, the model predicts large zone of distributed cracking above the loading point for high loading velocities. Strain rate dependency in constitutive load helps to reduce this cracking as well as smooth loading acceleration, however, these remedies lead to incorrect crack pattern in later stages of too low loading forces.

## 4.6 Spalling test

To investigate the model ability to predict material behavior at strain-rates higher than $10\,\mathrm{s}^{-1}$ test using Hopkinson pressure bar setup are simulated. It is used for estimation of dynamical tensile strength induced by spalling. Test series reported by [15, 14] was selected because of direct measurements of the rear face velocity, which is important for estimation of dynamic tensile strength.

The test setup consists of long metal (usually steel or aluminum alloy) bar and relatively short concrete cylinder at its end. Metal bar is loaded by impact of a projectile or by an explosive and the pressure wave propagates along the bar until it reaches its end. At the contact between metal and concrete, some part of pressure wave is reflected backwards to the metal bar as a tensile wave and the rest of it is transmitted into the concrete specimen, where it further propagates as a pressure wave. When it reaches the rear face of concrete cylinder, it is reflected as a tensile wave and, after reaching the material tensile strength, the specimen breaks.

To determine the dynamic tensile strength from results of SHPB test, theory derived for 1D longitudinal wave propagation according to [32] is usually applied. [14] use the following relation

$$f_{\mathrm{t,dyn}} = \frac{1}{2}\,\rho\, c\, \Delta V_{\mathrm{pb}} \tag{21}$$

where $\Delta V_{\mathrm{pb}}$ is pullback velocity, which is a difference between the maximum and *residual* velocity of the rear face of the specimen, $c$ is a wave speed, which can be for elastic materials analytically calculated

$$c = \sqrt{\frac{E(1-\nu)}{\rho(1+\nu)(1-2\nu)}} \tag{22}$$

Here $E$, $\nu$ and $\rho$ are macroscopic elastic modulus, Poisson's ratio and density respectively. Empirical determination of residual velocity is proposed in Sec. 4.6.2.

### 4.6.1 Wave propagation along elastic material

At first, propagation of a stress wave along elastic cylindrical bar was investigated, similarly to study done by [20]. Stress wave was prescribed according to one period of following cosine function

$$\sigma(t) = \begin{cases} \frac{1}{2}\left[\sigma_{\max} - \sigma_{\max}\cos\left(\frac{2\pi t}{t_{\mathrm{P}}}\right)\right] & \text{for } t \le t_{\mathrm{P}} \\ 0 & \text{for } t > t_{\mathrm{P}} \end{cases} \tag{23}$$

where $\sigma_{\max}$ is the peak stress applied and $t_{\mathrm{P}}$ is the period of the stress wave. Chosen parameters are: cylinder length $L = 400\,\mathrm{mm}$ and radius $R = 22.5\,\mathrm{mm}$, the maximum stress $\sigma_{\max} = 4\,\mathrm{MPa}$ and the period of imposed stress wave $t_{\mathrm{P}} = 50\,\mu\mathrm{s}$. The material parameters are following: $E_0 = 70\,\mathrm{GPa}$, $\alpha = 0.237$, $\rho = 2340\,\mathrm{kg/m^3}$ and $l_{\min} = 5\,\mathrm{mm}$.

In Fig. 14, results of elastic simulations are plotted. The graph on the left shows evolution of the rear face velocity in time and the graphs in the right part show the stress profile along the bar in four different times during the simulation. Even though the step length does not influence the stability of the solution, it influences its accuracy, as can be observed from slightly different results for various step length. The vertical lines in the left graph mark times when stress profiles are plotted. Thanks to the heterogeneous inner material structure represented by the model, the stress profile is not smooth. This can be observed in the upper right graph in Fig. 14 where nodal stress $\sigma_x$ of each particle is represented by a small dot. In the lower graphs, only the average stress in longitudinal bar direction is plotted. Averaging is performed in slices

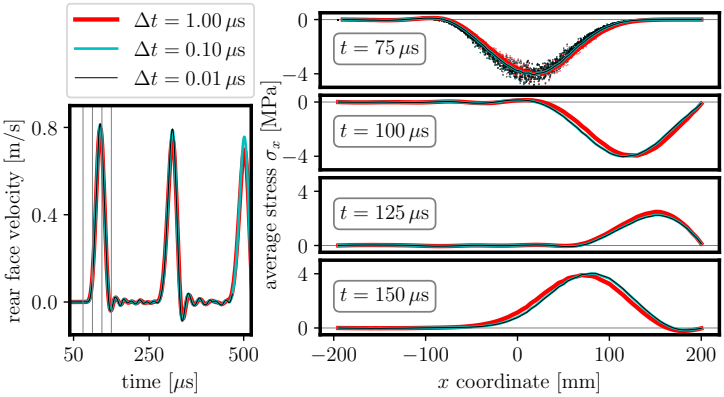


Figure 14: Results for different time step length $\Delta t$, left: rear face velocity evolution in time, right: stress profile along the elastic bar in particular times.

of width 5 mm, corresponding to parameter $l_{\text{min}}$ dictating the particle size. The wave speed obtained from the results of this test is $c_{\text{act}} \approx 4200\text{m/s}$.

### 4.6.2 Study of fracturing behavior

Prior to the comparison of the model with the experimental data, model behavior for this test setup was investigated also in nonlinear regime. Stress pressure wave used for this study is shown in left part of Fig. 15 as wave 3. Note that even for this reduced pressure wave, the strain-rate reaches value 20/s. Simulated specimen has length $L = 140\,\text{mm}$ and radius $R = 22.5\,\text{mm}$. Elastic material parameters and density for this preliminary study are same as in Sec. 4.6.1, parameters governing nonlinear part of constitutive law are $f_t = 8\,\text{MPa}$ and $G_f = 36.5\,\text{J/m}^2$. Parameters of rate dependency of are chosen according to recommendations in [9] $c_0 = 10^{-5}\,\text{s}^{-1}$ and $c_1 = 5 \cdot 10^{-2}$. The rear face velocity in time is plotted in right part of Fig. 15 for 6 different material models. The dynamic tensile strength is estimated using Eq. (21). Looking at the rear face velocity evolution, it is often unclear what value should be taken as pull-back velocity $\Delta V_{\text{pb}}$.

At first, let us focus on the response of the model with $0.25\,f_{\text{t}}$. This response deviates from the elastic even before the peak velocity, which is caused by the large damage during pressure wave propagation, see the crack in the right part

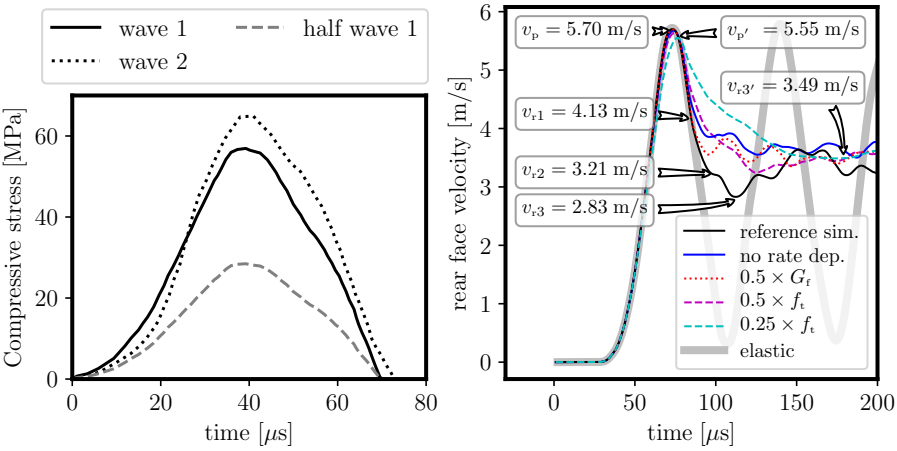


Figure 15: Left: Two stress waves reported by [15], wave 3 with half intensity of wave 1 is introduced for study of model behavior, right: study on various material model settings

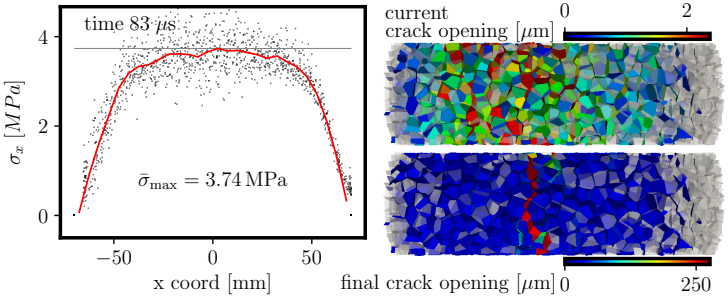


Figure 16: Stress profile along the specimen and crack pattern in time of maximum tensile $\sigma_x$ for simulation with $0.25 \times f_t$.

of Fig. 16. A lot of contacts are damaged already at the time of the peak stress. The stress profile is shown in the same figure, value of the peak stress $\bar{\sigma}_{max} = 3.74\,\text{MPa}$. Calculation of the dynamic strength considering the local minimum gives exaggerated value of $f_{t,dyn} = 9.88\,\text{MPa}$. The value obtained with consideration of the inflex point is $f_{t,dyn} = 2.58\,\text{MPa}$ which a bit lower than the model prediction, however it is much closer than the other one. The response of the material is highly influenced by the transverse damage due to

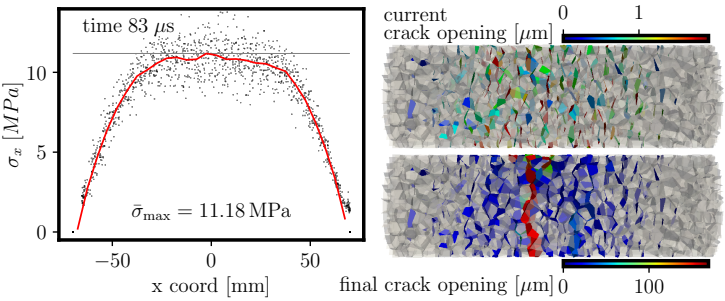


Figure 17: Stress profile along the specimen and crack pattern in time of maximum tensile $\sigma_x$ for reference simulation.

huge compressive loading (relative to the material strength). This corresponds with the recommendation reported by [17] which states that one should avoid pressures larger than 30% of compressive strength for this spalling test.

Now focus on the response of the reference material model. Also for this response, the value of dynamic tensile strength calculated using the velocity at the inflex point $f_{\mathrm{t,dyn}} = 12.12\,\mathrm{MPa}$ is closer to the value of maximum stress extracted from the meso-scale analysis $\bar{\sigma}_{\max} = 11.18\,\mathrm{MPa}$ (Fig. 17), the value considering local minimum if $f_{\mathrm{t,dyn}} = 13.82\,\mathrm{MPa}$.

### 4.6.3 Comparison to experimental data

Two tests were selected for comparison with results of the developed numerical model. Stress waves measured by [15] were used (Fig. 15). Concrete specimens had length $L = 140\,\mathrm{mm}$ and radius $R = 22.5\,\mathrm{mm}$. Specimens were made of saturated (wet) concrete with the following macroscopic parameters: elastic modulus $E = 42\,\mathrm{GPa}$, Poisson's ratio $\nu = 0.2$, density $\rho = 2380\,\mathrm{kg/m^3}$ and tensile strength $f_t = 3.7\,\mathrm{MPa}$.

The material parameters for the meso-scale model are following: elastic modulus $E_0 = 77\,\mathrm{GPa}$, parameter $\alpha = 0.1667$, density $\rho = 2380\,\mathrm{kg/m^3}$, tensile strength $f_{\mathrm{t}} = 3.7\,\mathrm{MPa}$ and fracture energy $G_{\mathrm{f}} = 36.5\,\mathrm{J/m^2}$. Parameters of rate dependency are $c_0 = 10^{-5}\,\mathrm{s^{-1}}$ and $c_1 = 10^{-1}$. Since the relation between macro and mesoscopic elastic properties – Eq. (8) – is only approximate, the actual mesoscale elastic modulus was identified from the wave speed and the maximum velocity of the rear face using wave 1. The resulting value $E_0 = 77\,\mathrm{GPa}$ is

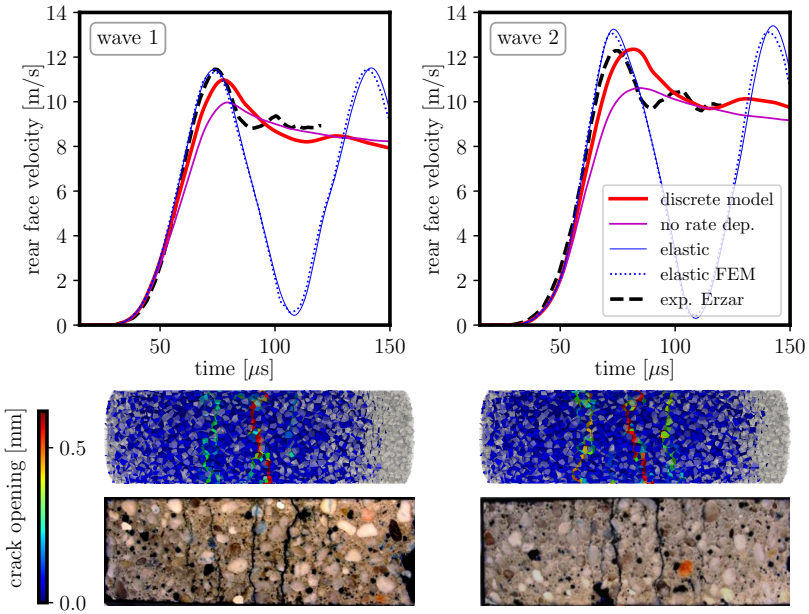


Figure 18: Results of numerical simulations compared to the experimental data by [15].

slightly higher than 70 GPa which would be value obtained by Eq. (8). This is in agreement [13], because Eq. (8) underestimates $E_0$ for positive Poisson's ratios. For verification, results of elastic FEM simulation with the macroscopic elastic modulus and Poisson's ratio is performed. The difference between continuous and discrete elastic simulation is negligible for both waves (Fig. 18) and the difference is attributed to different solution methods. The fracture energy $G_\mathrm{f}$ was chosen to obtain post peak evolution of the rear face velocity comparable to experimental data for the first loading case – wave 1. The second rate dependency parameter $c_1$ is increased for the same reason.

The model response for both loading cases along with experimental data [15] is shown in Fig. 18. It can be observed that the experimental peak velocity for wave 1 corresponds to the elastic response of the model. However, looking at the response for wave 2, the model elastic response of the same material is above the experimental peak velocity. It could possibly be explained by inelastic effects occurring in experiments during the pressure wave propagation,

which did not occur under lower pressure of wave 1.

The responses of nonlinear model deviate from elastic response prior to reaching peak velocity in both cases, again due to inelastic effects during compression phase. These effects are magnified when rate dependency is neglected. The descending part of the simulated pullback velocity line is not as steep as reported in experiments. There are multiple macrocracks created in the model, shown in the bottom part of Fig. 18, which corresponds to the experimental evidence [15].

# 5 Closing remarks

## 5.1 Conclusions about the fiber model

The parameters of the mathematical model are related to the actual physical phenomena of the material behavior at meso-scale. Even if the fibers are represented indirectly, the constitutive law contains information about their behavior during loading. Experimental data on a single fiber pullout [42, 37, 35] as well as on whole specimens made of fiber reinforced composite [27, 44] are broadly reported in literature, however, the connection between them is missing. For example the correlation between concrete strength on one side and bond and frictional fiber characteristics on the other side would be extremely helpful.

The numerical model is able to represent the fiber reinforced composites behavior, strain-hardening after the initial cracking and also multiple cracks are captured. However, the parameters used for the numerical model are quite different compared to those reported experimentally.

## 5.2 Conclusions about the dynamic model

Application of the discrete meso-scale model showed the model ability to imitate the dynamic concrete behavior. The model is, up to some point, able to reproduce both major attributes of the rate dependent concrete behavior, increase in loading forces and changes in the crack pattern. Initially, these were attributed to the heterogeneous material structure and its direct representation in the meso-scale model should have ensured capturing all the rate-dependency. This idea turned out to be too ambitious and rate-dependency of the constitu-

tive law needed to be incorporated to enable more appropriate representation of material behavior, especially for high strain-rates.

The direct application of the displacement under higher strain rates resulted in crushing of the material close to the loading point. This occurred even though the displacement was applied via rigid plate and not in a single point. Various remedies were tried to fix this behavior, e.g. gradual increase in displacement rate instead of loading under full velocity from the beginning. These helped to prevent crushing, however, the increase in loading forces was lost due to reduced inertia effect.

The developed model was used to determine the macro-scopic homogeneous model characteristics in [25]. Dependency of the process zone size and other characteristics on the strain rate and specimen size was investigated on a small specimens representing ceramics at fine resolution, using the presented model. The specimens were loaded in tension, random field was considered.

## 5.3 Future work

The discrete meso-scale model appears to be capable of representing the complex behavior of heterogeneous cement-based composite. This representation is, however, limited.

The limits of the current model configuration reveal the space for the future modifications. For example the transition from tensile into compressive loading that happens during reflection of the wave at the domain boundary, results into the loading unloading cycle. The constitutive law governed by the damage variable lacks representation of irreversible strain, model gives zero strain when fully unloaded. So the next step is modification of the constitutive law for more realistic representation of loading-unloading cycles.

Opportunity also lies in the application of the model to other materials or structures at different scales. For example, low-scale representation of masonry structures is a challenging task that the author considers to investigate further.

# References

[1] *CEB-FIP MODEL CODE*, 2. Material Properties, s. 33–81. 1990. doi:10.1680/ceb-fipmc1990.35430.0002.

[2] Adendorff, C. – Boshoff, W. – Zijl, G. Characterisation of crack distribution of Strain-Hardening Cement Composites (SHCC) under imposed strain. *Advances in Cement-Based Materials*. 2009, s. 215–221. doi:10.1201/b10162-32.

[3] Aïtcin, P.-C. 4 - Supplementary cementitious materials and blended cements. In Aïtcin, P.-C. – Flatt, R. J. (Ed.) *Science and Technology of Concrete Admixtures*. Woodhead Publishing, 2016. s. 53 – 73. doi:https://doi.org/10.1016/B978-0-08-100693-1.00004-7. ISBN 978-0-08-100693-1.

[4] Bathe, K.-J. *Finite element procedures*. Prentice Hall, 1996. ISBN 01-330-1458-4.

[5] Bažant, Z. P. – Lin, F. Nonlocal Smeared Cracking Model for Concrete Fracture. *Journal of Structural Engineering*. 1988, 114, 11, s. 2493–2510. ISSN 0733-9445. doi:10.1061/(ASCE)0733-9445(1988)114:11(2493).

[6] Bažant, Z. – Oh, B. Crack band theory for fracture of concrete. *Matériaux et Constructions*. 1983, 16, 3, s. 155–177. ISSN 0025-5432. doi:10.1007/BF02486267.

[7] Bentur, A. – Mindess, S. *Fibre reinforced cementitious composites*. 2nd ed edition, 2007. ISBN 978–0–415–25048–1.

[8] Brara, A. – Klepaczko, J. Experimental characterization of concrete in dynamic tension. *Mechanics of Materials*. 2006, 38, 3, s. 253–267. ISSN 01676636. doi:10.1016/j.mechmat.2005.06.004.

[9] Cusatis, G. Strain-rate effects on concrete behavior. *International Journal of Impact Engineering*. 2011, 38, 4, s. 162–170. doi:10.1016/j.ijimpeng.2010.10.030.

[10] Cusatis, G. – Cedolin, L. Two-scale study of concrete fracturing behavior. *Engineering Fracture Mechanics*. 2007, 74, 1-2, s. 3–17. doi:10.1016/j.engfracmech.2006.01.021.

[11] Cusatis, G. – Bažant, Z. P. – Cedolin, L. Confinement-Shear Lattice Model for Concrete Damage in Tension and Compression. *Journal of Engineering Mechanics*. 2003, vol. 129, 12, s. 1439–1448. ISSN 0733-9399. doi:10.1061/(ASCE)0733-9399(2003)129:12(1439).

[12] Eibl, J. – Schmidt-Hurtienne, B. Strain-Rate-Sensitive Constitutive Law for Concrete. *Journal of Engineering Mechanics*. 1999, vol. 125, 12, s. 1411–1420. ISSN 0733-9399. doi:10.1061/(ASCE)0733-9399(1999)125:12(1411).

[13] Eliáš, J. Boundary Layer Effect on Behavior of Discrete Models. *Materials*. 2017, 10, 2, s. 157. ISSN 1996-1944. doi:10.3390/ma10020157.

[14] Erzar, B. – Forquin, P. An Experimental Method to Determine the Tensile Strength of Concrete at High Rates of Strain. *Experimental Mechanics*. 2010, 50, 7, s. 941–955. ISSN 0014-4851. doi:10.1007/s11340-009-9284-z. Dostupné z: <http://link.springer.com/10.1007/s11340-009-9284-z>.

[15] Erzar, B. – Forquin, P. Experiments and mesoscopic modelling of dynamic testing of concrete. *Mechanics of Materials*. 2011, 43, 9, s. 505–527. ISSN 01676636. doi:10.1016/j.mechmat.2011.05.002.

[16] Fantilli, A. P. – Mihashi, H. – Vallini, P. Multiple cracking and strain hardening in fiber-reinforced concrete under uniaxial tension. *Cement and Concrete Research*. 2009, 39, 12, s. 1217–1229. ISSN 00088846. doi:10.1016/j.cemconres.2009.08.020.

[17] Forquin, P. – Riedel, W. – Weerheijm, J. Chapter 6 - Dynamic test devices for analyzing the tensile properties of concrete. In Weerheijm, J. (Ed.) *Understanding the Tensile Properties of Concrete*, Woodhead Publishing Series in Civil and Structural Engineering. Woodhead Publishing, 2013. s. 137 – 181. doi:https://doi.org/10.1533/9780857097538.2.137. ISBN 978-0-85709-045-4.

[18] Fowler, A. C. – Scheu, B. A theoretical explanation of grain size distributions in explosive rock fragmentation. *Proceedings of the Royal Society A: Mathematical, Physical and Engineering Science*. 2016, vol. 472, issue 2190, s. 20150843–. ISSN 1364-5021. doi:10.1098/rspa.2015.0843.

[19] Grassl, P. et al. Meso-scale modelling of the size effect on the fracture process zone of concrete. *International Journal of Solids and Structures*. 2012, vol. 49, 13, s. 1818–1827. ISSN 00207683. doi:10.1016/j.ijsolstr.2012.03.023. Dostupné z: <http://linkinghub.elsevier.com/retrieve/pii/S0020768312001175>.

[20] Hwang, Y. K. – Bolander, J. E. – Lim, Y. M. Simulation of concrete tensile failure under high loading rates using three-dimensional irregular lattice models. *Mechanics of Materials*. 2016, 101, s. 136–146. ISSN 0167-6636. doi:10.1016/j.mechmat.2016.08.002.

[21] Jirásek, M. Nonlocal models for damage and fracture: comparison of approaches. *Solid Structures*. 1998, 35, s. 4133–4145.

[22] Jirásek, M. – Bažant, Z. P. Particle Model for Quasibrittle Fracture and Application to Sea Ice. *J. Eng. Mech.* 1995, 121, 9, s. 1016–1025. doi:10.1061/(asce)0733-9399(1995)121:9(1016).

[23] Kang, J. et al. Modeling of fiber-reinforced cement composites: Discrete representation of fiber pullout. *International Journal of Solids and Structures*. 2014, 51, 10, s. 1970 – 1979. ISSN 0020-7683. doi:10.1016/j.ijsolstr.2014.02.006.

[24] Kawai, T. New discrete models and their application to seismic response analysis of structures. *Nuclear Engineering and Design*. 1978, 48, 1, s. 207 – 229. ISSN 0029-5493. doi:https://doi.org/10.1016/0029-5493(78)90217-0. Special Issue Structural Mechanics in Reactor Technology - Smirt-4.

[25] Le, J.-L. et al. Rate-Dependent Scaling of Dynamic Tensile Strength of Quasibrittle Structures. *Journal of Applied Mechanics*. 2018, 85, 2. ISSN 0021-8936. doi:10.1115/1.4038496.

[26] Leppänen, J. Concrete subjected to projectile and fragment impacts. *International Journal of Impact Engineering*. 2006, vol. 32, 11, s. 1828–1841. ISSN 0734743x. doi:10.1016/j.ijimpeng.2005.06.005.

[27] Li, V. C. et al. Tensile strain-hardening behavior of polyvinyl alcohol engineered cementitious composite (PVA-ECC). *ACI Materials Journal-American Concrete Institute*. 2001, 98, 6, s. 483–492.

[28] Li, V. C. et al. Interface tailoring for strain-hardening polyvinyl alcohol-engineered cementitious composite (PVA-ECC). *Materials Journal*. 2002, 99, 5, s. 463–472.

[29] Mellinger, F. – Birkimer, D. Measurements of stress and strain on cylindrical test specimens of rock and concrete under impact loading. Technical report, Ohio River Div Labs Cincinnati, 1966.

[30] Naaman, A. E. et al. Fiber Pullout and Bond Slip. I: Analytical Study. *Journal of Structural Engineering*. 1991, 117, 9, s. 2769–2790. doi:10.1061/(ASCE)0733-9445(1991)117:9(2769).

[31] Newmark, N. *A method of computation for structural dynamics*. University of Illinois, 1959.

[32] Novikov, S. – Divnov, I. – Ivanov, A. Investigation of the fracture of steel, aluminum and copper during explosive loading. *Fiz Metallov Metalloved*. 1966, 21, 4, s. 608–615.

[33] Ožbolt, J. et al. Dynamic fracture of concrete L-specimen. *Engineering Fracture Mechanics*. 2015, vol. 148, s. 27–41. ISSN 00137944. doi:10.1016/j.engfracmech.2015.09.002.

[34] Ožbolt, J. – Sharma, A. – Bede, N. Dynamic Fracture of L and CT Concrete Specimens. *Proceedings of the 9th International Conference on Fracture Mechanics of Concrete and Concrete Structures*. 2016. doi:10.21012/FC9.098.

[35] Redon, C. et al. Measuring and Modifying Interface Properties of PVA Fibers in ECC Matrix. *Journal of Materials in Civil Engineering*. 2001, 13, 6, s. 399–406. ISSN 0899-1561. doi:10.1061/(ASCE)0899-1561(2001)13:6(399).

[36] Schauffert, E. A. – Cusatis, G. Lattice Discrete Particle Model for Fiber-Reinforced Concrete. I. *Journal of Engineering Mechanics*. 2012, 138, 7, s. 826–833. ISSN 0733-9399. doi:10.1061/(ASCE)EM.1943-7889.0000387.

[37] Scheffler, C. et al. Poly (vinyl alcohol) fiber reinforced concrete: investigation of strain rate dependent interphase behavior with single fiber pullout test under quasi-static and high rate loading. *Journal of Adhesion Science and Technology*. 2013, 27, 4, s. 385–402.

[38] Schuler, H. – Hansson, H. Fracture behavior of High Performance Concrete (HPC) investigated with a Hopkinson-Bar. *http://dx.doi.org/10.1051/jp4:2006134175*. 08 2006, 134. doi:10.1051/jp4:2006134175.

[39] Tonon, F. Explicit Exact Formulas for the 3-D Tetrahedron Inertia Tensor in Terms of its Vertex Coordinates. *Journal of Mathematics and Statistics*. 2005, 1, 1, s. 8–11. ISSN 15493644. doi:10.3844/jmssp.2005.8.11.

[40] Mier, J. G. M. *Concrete fracture*. CRC Press, 2013.

[41] Weerheijm, J. – Doormaal, J. V. Tensile failure of concrete at high loading rates: New test data on strength and fracture energy from instrumented spalling tests. *International Journal of Impact Engineering*. 2007, 34, 3, s. 609 – 626. ISSN 0734-743X. doi:https://doi.org/10.1016/j.ijimpeng.2006.01.005.

[42] Yang, E.-H. et al. Fiber-Bridging Constitutive Law of Engineered Cementitious Composites. *Journal of Advanced Concrete Technology*. 2008, 6, 1, s. 181–193. ISSN 1346-8014. doi:10.3151/jact.6.181.

[43] Yang, E.-H. et al. Fiber-bridging constitutive law of engineered cementitious composites. *Journal of advanced concrete technology*. 2008, 6, 1, s. 181–193.

[44] Zhou, J. et al. Development of engineered cementitious composites with limestone powder and blast furnace slag. *Materials and Structures*. 2010, 43, 6, s. 803–814. ISSN 1359-5997. doi:10.1617/s11527-009-9549-0.

# Josef Květoň *January 5, 1989*

kveton.j@fce.vutbr.cz • +420 541147131
Institute of Structural Mechanics • Faculty of Civil Engineering • Brno University of Technology
Veveří 331/95 • 602 00 Brno • Czech Republic


## Current possition

Brno University of Technology, Faculty of Civil Engineering — Brno, Czech Republic
**Doctoral Student** — *Feb '15 – present*
Discrete approach in damage mechanics
Teaching experience: *Fundamentals of Structural Mechanics*, *Structural Analysis II*, (Czech)

## Education

Brno University of Technology, Faculty of Civil Engineering — Brno, Czech Republic
**Master degree in Civil Engineering** — *2013 – 2015*
Thesis "Simulation of Concrete Fracture Using Nonlocal Model"

Brno University of Technology, Faculty of Civil Engineering — Brno, Czech Republic
**Bachelor degree in Civil Engineering** — *2009 – 2013*
Thesis "Comparison of Loacalization Limiters for Strain - Softening"

## International Activities

Delft University of Technology, Faculty of Civil Engineering and Geosciences — Delft, Netherlands
**Erasmus+ Internship** — *Jan – July 2018*
Simulations of Fiber Reinforced Composites

## Courses attended

Gopas — Brno, Czech Republic
**Object oriented programming in C++** — *Oct '16*

International Center for Mechanical Sciences — Udine, Italy
**Modeling, Simulation and Characterization of Multi-Scale Heterogeneous Materials** — *Sept '15*

BOKU University — Vienna, Austria
**Multi-Scale and Multi-Phase Modeling of Aging Concrete Structures** — *June 15*

BOKU University — Vienna, Austria
**Advanced Topics in Engineering Mechanics** — *June 15*

Czech Technical University, Faculty of Civil Engineering — Prague, Czech Republic
**Modeling of Localized Inelastic Deformation** — *Sept '14*

## Participation in research projects

**GA19-12197S** — *2019 – present*
**Coupled discrete meso-scale model for mechanics and transport phenomena in concrete**

**GA19-06684J** — *2019 – present*
**Fatigue of structural concrete driven by cumulative measure of shear strain**

**FAST-J-18-5412** — 2018
**Short fiber reinforcement in discrete meso-scale model** — *Principal investigator*

**FAST-J-17-4583** — **2017**
**Strain-rate effect in concrete fracture** — *Principal investigator*

**GJ15-19865Y** — *2016–2017*
**Discrete fracture models: adaptive remeshing, energy release rate, and stress along boundaries**

**Specialization, research interests:** Computational Mechanics, Nonlinear Material Modeling, Fracture Mechanics, Localization Limiters, Discrete Models, Strain-rate Effect, Fiber Reinforcement

**Computer skills:** Structural design software Ansys/Scia/Rfem/Atena, CAD software, Office packages, LaTeX, Programing languages Python/C++.

**Languages:** Czech *(native)*, English *(upper intermediate)*, German *(intermediate)*.

**Interests:** Scouting, Futsal, Trekking, Mountain Climbing, Skiing, Cycling, Motorbikes, Archery

## List of Publications


KVĚTOŇ, J., ELIÁŠ, J. Influence of inertia and material properties on discrete simulation of dynamic fracture of concrete. *Procedia Structural Integrity*, 13:1367 – 1372, 2018a. ISSN 2452-3216. doi: https://doi.org/10.1016/j.prostr.2018.12.286. ECF22 - Loading and Environmental effects on Structural Integrity.

LE, J.-L., ELIÁŠ, J., GORGOGIANNI, A., VIEVERING, J., KVĚTOŇ, J. Rate-dependent scaling of dynamic tensile strength of quasibrittle structures. *Journal of Applied Mechanics, Transactions ASME*, 85(2), 2018b. doi: 10.1115/1.4038496.

KVĚTOŇ, J., ELIÁŠ, J. Simulations of dynamic concrete fracture with brazilian splitting test. In *Proceedings of the International Conference on Computational Methods*, 13, pages 1367 – 1372. Scien Tech Publisher, 2018c.

KVĚTOŇ, J., ELIÁŠ, J. Simulations of concrete fracture at various strain rates: Parametric study. In *COMPDYN 2017 - Proceedings of the 6th International Conference on Computational Methods in Structural Dynamics and Earthquake Engineering*, 2, pages 4847–4856, 2017d. doi: 10.7712/120117.5766.17557.

KVĚTOŇ, J., ELIÁŠ, J. Discrete modeling of strain rate effect in concrete fracture. *Key Engineering Materials*, 754 KEM:345–348, 2017e. doi: 10.4028/www.scientific.net/KEM.754.345.

KVĚTOŇ, J., ELIÁŠ, J. Vliv rychlosti zatěžování na porušení betonu: Numerická studie využívající diskrétní model. In *Sborník doktorandské konference k 95. výročí kloknerova ústavu*, 2016f. ISBN 978-80-248-3917-2.

KVĚTOŇ, J., ELIÁŠ, J. Study of the nonlocal model parameters dependency. In *Proceedings of 18th International Conference of PhD students Juniorstav*, 2016g. ISBN 978-80-214-5311-1.

KVĚTOŇ, J., ELIÁŠ, J. Identification of material parameters for nonlocal model of concrete fracture. In *Proceedings of the Fifteenth International Conference on Civil, Structural and Environmental Engineering Computing*. Civil-Comp Press, 2015h. doi: 10.4203/ccp.108.24.

KVĚTOŇ, J., ELIÁŠ, J. Simulation of fracture experiments on concrete using nonlocal damage model. In *Proceedings of 13th International Conference Modeling in Mechanics*, 2015i. ISBN 978-80-248-3756-7.

KVĚTOŇ, J., ELIÁŠ, J. Performance comparison of localization limiters. In *Proceedings of 20th Interantional Conference Engineering Mechanics*, 2014j. ISBN 978-80-214-4871-1.

# Abstract

The presented thesis is devoted to mathematical modeling of concrete fracture. A special type of model called discrete particle model is used. The concrete meso-structure is simplified as a system of interconnected polyhedral particles. The particles represent larger concrete aggregates with surrounding cement paste. The particle interaction is prescribed at their contacts. Solution of discrete displacement field is obtained under the assumption of small deformations and rigid body movement of particles. Two modifications of the static version of the discrete meso-scale model are presented: (i) representation of short fiber reinforcement and (ii) implicit dynamic solver.

The first main part of the thesis is devoted to modelling of short fiber reinforcement, which is used to improve poor tensile performance of concrete. This material modification leads to more efficient material use and crack width reduction. Short fibers are represented in the discrete model indirectly, taking into account the frictional forces between fiber and cement matrix. The fiber forces are applied at particle contacts working against the crack opening. This modification is able to capture the strain hardening behavior and the multiple cracking of the fiber reinforced composites.

The second main part of the thesis addresses dynamic material behavior. Concrete resistance varies under different strain-rates. For slow, quasi-static loading rates, the initial micro-cracks localize into a macro-crack. For fast loading rates, the energy is not consumed by one crack only, but multiple cracking and crack branching occurs. The inertia typically dominates in fast processes. Even though the meso-scale model accounts for the inertia and the crack branching, the cracking at lower scale is not addressed. Therefore additional phenomenological rate-dependency of the constitutive law is adopted. Numerical simulations on various geometries under various loading rates are performed and compared to experimental evidence from literature. Dynamic material behavior is computed using Newmark's implicit time-integration scheme.